Aerodynamics of aerofoil sections measured on a free-flying bird

A C Carruthers*, **S M Walker, A L R Thomas,** and **G K Taylor**
Department of Zoology, University of Oxford, Oxford, UK

The manuscript was received on 28 October 2009 and was accepted after revision for publication on 17 December 2009.

DOI: 10.1243/09544100JAERO737

Abstract: Birds are adapted to a wide range of flight conditions, from steady fixed-wing glides to high angle of attack manoeuvres involving unsteady separated flows. They naturally control and exploit the transitional Reynolds number regime of $Re \approx 10^5$ that is currently of interest in unmanned air vehicle technologies. This article presents a reconstruction of the inner portion of a wing of an eagle in free flight, during a rapid pitch-up manoeuvre at the end of a shallow glide to an elevated perch. Photogrammetric techniques were used to map the identified points on the wing and these were used to fit a mathematical model of the upper and lower surface topography using polynomial regression techniques. The surface model accounts for spanwise twist, spanwise bending, and varying chord distribution, as well as for the shape of the aerofoil. The aerodynamics of the two-dimensional aerofoil sections were analysed using XFOIL and were compared against two technical aerofoils, namely the Selig S1223 and Clark Y aerofoils, at $1 \times 10^5 \leqslant Re \leqslant 2 \times 10^5$. The bird aerofoil maintains a robust, near-constant drag coefficient over a wide lift coefficient range.

Keywords: bird flight, low Reynolds number, wing reconstruction

1 INTRODUCTION

In recent years, birds have become of increasing interest to engineers developing unmanned air vehicles (UAVs). They have naturally evolved to fly within a similar transitional Reynolds number regime ($Re \approx 10^5$), and are adapted to a wide range of similar flight conditions – from steady fixed-wing glides to high angle of attack manoeuvres involving unsteady separated flows. A key difference between birds and conventional UAVs is that their wings have specifically evolved to deform in flight, under a combination of muscular, elastic, and aerodynamic loading. Surprisingly, however, there have not been any accurate measurements of the wing profiles of comparable sized birds under natural flight conditions. In consequence, there is a lack of knowledge about even the most fundamental aerodynamic parameters characterizing the performance of the aerofoil sections of real birds in free flight. This article presents measurements of the detailed wing shape of a bird flying freely under natural conditions outdoors and provides a computational aerodynamic analysis of the performance of the measured aerofoil sections.

Bird wing profiles and planforms have typically been measured from museum specimens [**1**], which exhibit distortions due to curing and preservation. Measurements of wing sections from recently deceased birds [**2**] suffer similar problems, according to how the wing is set. The measured profiles typically have very poor aerodynamic characteristics [**1**] and are unlikely to represent accurately the shape of the wing under aerodynamic loading, which can only be measured reliably from free-flying birds. Early work by Nachtigall and Wieser [**3**] used multiple camera photogrammetry to reconstruct pigeon wing profiles from recently deceased birds. Work by Bilo [**4**, **5**] used stereophotogrammetry to reconstruct the shape of the upper wing surface of a House Sparrow *Passer domesticus* during flapping flight in a small wind tunnel. Later work by Brill *et al.* [**6**] used two stereo cameras to measure the aerofoil sections of a European Starling *Sturnus vulgaris* gliding in a wind tunnel [**6**]. These are probably the most accurate measurements of bird wing profiles that have previously been made, but the

**Corresponding author: Department of Zoology, University of Oxford, South Parks Road, Oxford, OX1 3PS, UK.*
email: anna.carruthers@zoo.ox.ac.uk

starling is a small bird (0.4 m wing span), which operates at Reynolds numbers below the transitional range that is of interest for the current generation of UAVs.

In this article, multi-station photogrammetry using six high-resolution digital cameras is used to reconstruct the three-dimensional (3D) upper and lower surface topography of the wing of a Steppe Eagle *Aquila nipalensis* during a rapid pitch-up manoeuvre at the end of a shallow glide to an elevated perch. Representative 2D aerofoil sections are extracted, and their aerodynamic performance is analysed using a standard computational code. The performance of the measured bird-wing aerofoil sections is compared with that of two technical aerofoils: Clark Y, which is a standard and well-known section, and Selig S1223, which is designed as a high-lift aerofoil for flight at low Reynolds numbers.

2 MATERIALS AND METHODS

2.1 Animals

A trained, captive four-year-old male Steppe Eagle *Aquila nipalensis* (Hodgson) was used for all the flight tests. The bird has a body mass of 2.5 kg, a wing span of 2 m from tip to tip, and a mean wing chord of 0.3 m. The experimental protocol was approved by the Surgeon General's Human and Animal Research Panel, United States Air Force, in addition to the Local Ethical Review Committee, Department of Zoology, Oxford University, and was considered not to pose any significant risk of causing pain, suffering, damage or lasting harm to the animal involved.

2.2 Cameras

Six Canon EOS 30D SLR cameras (Canon Inc., Tokyo, Japan) were positioned around a measurement control volume through which the bird flew as it approached an elevated perch. The cameras were placed immediately in front of the perch, so as to allow the bird to land into the wind. The cameras were arranged in pairs to capture images of the upper surface, lower surface, and leading edge of the right wing. The cameras had a resolution of 3504×2336 pixels, were operated with a 1 ms exposure time, and were synchronized to within 2 ms. A high definition digital video camera (Sony Handycam HDR-SR1E, Sony Corporation, Tokyo, Japan) was used to record each perching sequence at 25 frames per second to provide the context for the sets of

Fig. 1 Set of six simultaneous images used for 3D wing reconstruction

still images. The test volume was calibrated using a patterned 2D calibration grid that was held in the measurement volume in a variety of different positions and orientations. A plumb line was used in calibration as a reference for the vertical.

2.3 Flight experiments

Testing was conducted outdoors in an open field near Abergavenny, Wales, between 12 November and 16 November 2007. The bird was released at a distance of approximately 100 m from the perch, to which it flew in order to receive a food reward. The cameras were positioned around a measurement volume immediately in front of the perch, so they captured the final stages of the perching manoeuvre.

A perching sequence typically involves a three-phase approach, comprising a fixed-wing glide low to the ground, followed by a rapid pitch-up manoeuvre, and finally a deep stall [**7**]. The wing operates at a very high angle of attack ($\alpha \approx 50^{\circ}$) during the pitch-up manoeuvre, and takes a very large positive aerodynamic load. Since these are the conditions of greatest interest for UAV design, it is during the rapid pitch-up manoeuvre that the images used here were captured (Fig. 1). In total, 108 sets of images were recorded from a total of 60 different landing sequences. Here, the data from a single image set, chosen as being representative of a typical pitch-up manoeuvre, will be analysed in detail [**7**].

2.4 Photogrammetric reconstruction technique

The 3D positions of points on the wing's surface were reconstructed from the 2D camera images using a photogrammetric software developed and written within the Department of Zoology, using MATLAB v. 7.4. Originally developed for the reconstruction of the wings of flying insects [**8**], this software has since been adapted for larger scale use on birds in a remote, outdoor environment. The calibration images of a 2D target grid were analysed using a non-linear least squares bundle adjustment to jointly optimize the camera optical parameters and the reconstructed positions of the calibration points. The reader is referred to Walker *et al.* [**8**] for further technical details of the calibration technique.

Natural features on the wing, such as feather tips and pigmentation, were then identified and matched manually between images. Overall image levels of brightness and contrast were adjusted for ease of viewing, but no further image processing was applied. The calibrated camera collinearity equations [**9**] were then solved to reconstruct the 3D positions of 390 identified target points (Fig. 2). The identified target points on the upper wing surface were distributed across the entire chord from the leading to the trailing edge, while

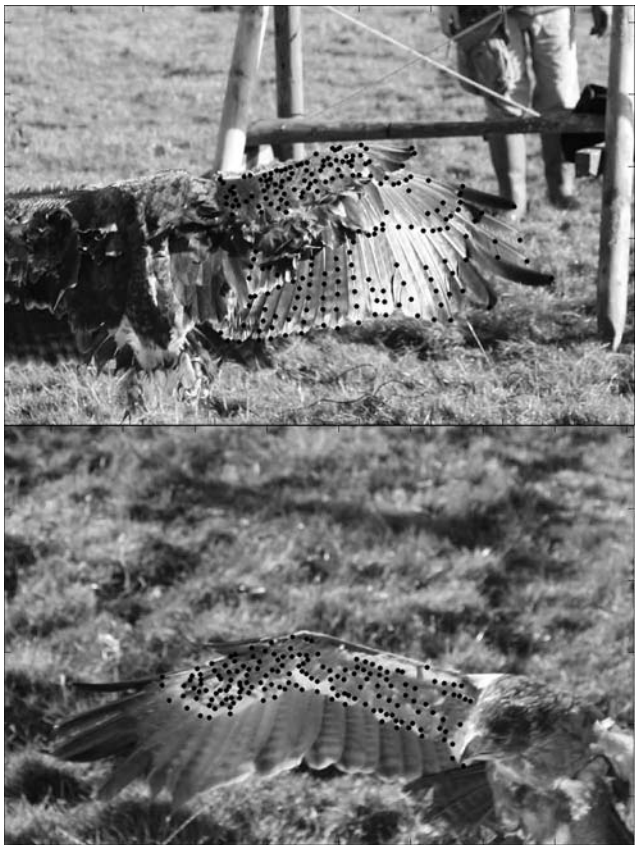

Fig. 2 Identified features on the bird's wing, shown as black spots

points on the lower surface were only identified over the thick forward portion of the wing, and not on the thin rear portion made up only of secondary feathers. The resulting 3D target points have a mean absolute 3D error of 4.31 mm; Walker *et al.* [**8**] describe the error estimate method in detail.

2.5 Mathematical model of the wing's surface

The 390 reconstructed target points form a dense cloud (Fig. 3(a)), from which it was necessary to construct a spatially averaged surface in order to be able to make useful estimates of aerodynamic performance. This was achieved using polynomial regression techniques in MATLAB to fit a smooth surface to the 252 points on the inner portion of the wing. This inner portion is known anatomically as the arm wing and is responsible for a majority of the lift production. The leading edge of the arm wing is arc-shaped, so in order to fit a representative series of aerofoil sections, it was necessary first to normalize the chord distribution. This was done by fitting a second-order polynomial to predict the spanwise curvatures of the leading and the trailing edge, respectively. The chordwise position of the individual target points was then adjusted using these polynomials by applying, first,

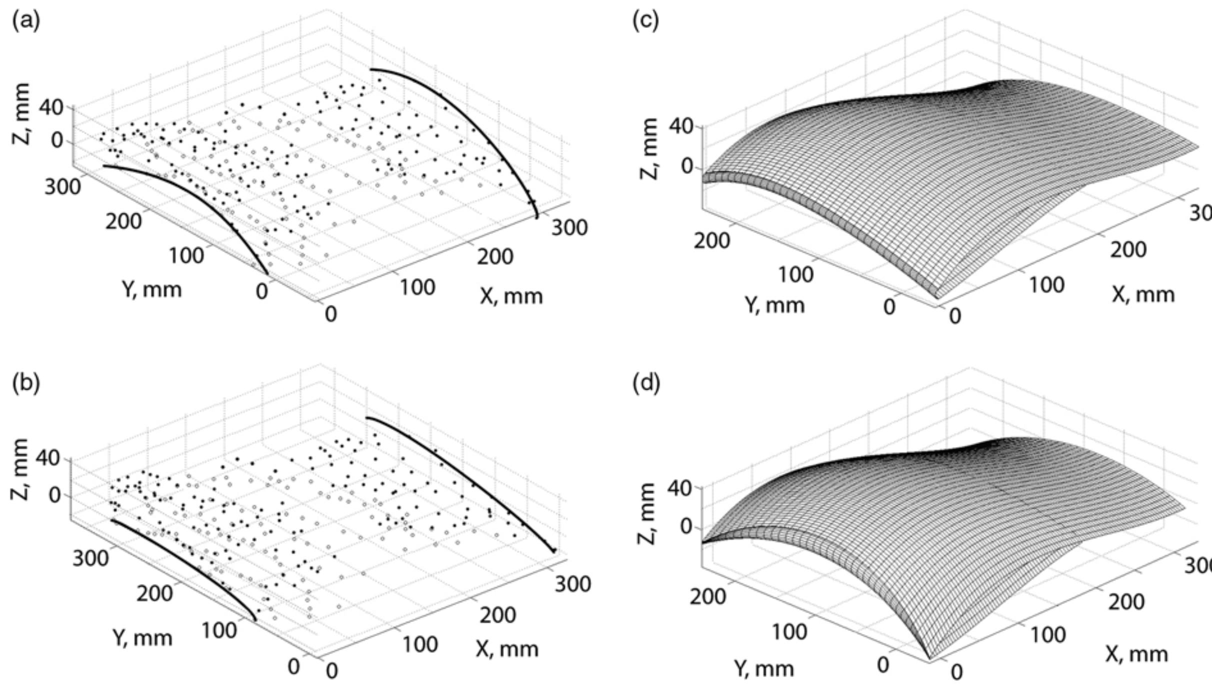

Fig. 3 Schematic diagram showing the data transformations involved in the wing reconstruction technique. Unfilled circles represent points on the lower surface; filled circles represent points on the upper surface. The leading edge of the wing is to the left: (a) view of the identified points on the wing's surface, as measured in a real-world coordinate system. The curved lines denote the second order polynomials fitted to the leading and trailing edges; (b) view of the identified points on the wing surface after transforming the coordinate system by translating the points at every spanwise station in a chordwise direction so as to straighten the leading edge; (c) surface reconstruction of the wing in the transformed coordinate system with straight leading edge and constant chord. The aerofoil section is the same at all spanwise stations in this transformed coordinate system, and is referred to as the 'standard' bird aerofoil in the text; and (d) surface reconstruction of the wing after back-transformation to the real-world coordinate system. The aerofoil sections described as 'squashed' and 'elongated' in the text are those at 35 per cent and 84 per cent of the span, respectively

a chordwise translation and, second, a chordwise stretch, to give a rectangular, rather than curved, wing planform (Fig. 3(b)). Since no transformation was applied to the height of the individual target points, the resulting rectangular planform retains the same arched form as the untransformed wing (Fig. 3(c)).

Polynomial regression techniques were then used to model the height (Z-coordinate) of all 252 target points on the arm wing as a polynomial function of their spanwise position (Y-coordinate), their normalized chordwise position (X-coordinate), and a dummy variable indicating whether the point fell on the upper or lower wing surface. The regression was able to predict 92 per cent of the variation in the vertical positions of the target points by modelling the curvature of the upper and lower aerofoil surfaces, respectively, as third-order polynomials of normalized chordwise position, with a linear spanwise twist distribution, and a fourth order spanwise bending distribution. These were chosen as the highest order polynomials for which all of the terms were statistically significant ($p < 0.05$).

The third-order models of the curvature of the upper and lower surfaces of the wing accurately captured the shape of the aerofoil over most of the chord, but were not of sufficiently high order to predict the shape of the rounded leading edge of the real wing. A Bezier function was therefore used to simulate the leading edge. This method is somewhat arbitrary, but there are too few easily identifiable points on the leading edge of the wing to enable a more accurate kind of modelling. Since it was not possible to measure the thickness of the thin rear portion of the wing using photogrammetric techniques, the thickness of the secondary feathers was measured directly and found to be of the order of 1 mm across this whole region, so 1 mm thickness was assumed for the rear portion of the wing. In reality, the secondaries slide over each other

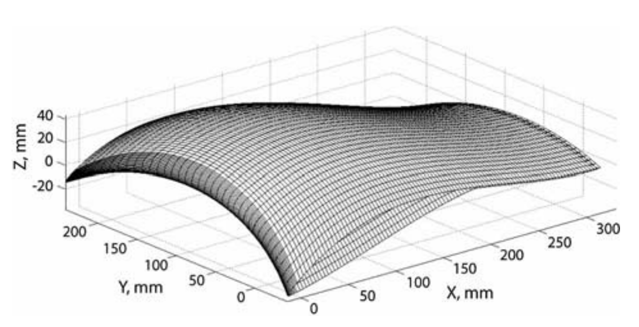

Fig. 4 Detailed view of wing surface reconstruction after back transformation to the real-world coordinate system, the Bezier function fit at the leading edge, and the 1 mm thickness over the rear portion of the wing

as the bird adjusts its wing geometry, so the thickness varies.

Finally, a back-transformation was applied to the regression surfaces using the polynomials that had been used earlier to normalize the chord distribution of the identified target points. This gave a curved wing planform that accurately modelled the curvature of the leading and trailing edges of the real wing (Figs 3(d) and 4).

2.6 XFOIL test cases

An open-source panel code (XFOIL 6.9.4) was used to predict the aerodynamic characteristics of the aerofoil section fitted in the regression on the data with normalized chord distribution (Fig. 5(a)). Hereafter, this section will be referred to as the 'standard' aerofoil section, because it represents a standardized average profile for the entire arm wing. Back-transformation of the regression surfaces to give a curved wing planform (see section 2.5) entails stretching the aerofoil in a chordwise direction, and this is used to bracket the performance of the standard aerofoil by also predicting the aerodynamic performance of the stretched profiles at 35 per cent and 84 per cent of the span. These are squashed and elongated, respectively, in comparison with the standard aerofoil (Fig. 5(b) and (c)). Squashing the aerofoil increases its thickness-to-chord ratio, and also increases its camber relative to the standard aerofoil section. Elongating the aerofoil has the opposite effect.

XFOIL is an open-source code [**10**] and is well recognized as a design and analysis tool for the optimization of 2D aerofoil sections [**11**, **12**]. It solves the potential equation using a second-order panel method with linear vortex variation distribution and a coupling between the external flowfield and viscous sub-layer. An e^N-method is used for the prediction of transition [**13**], and an amplification factor of $N_{\text{crit}} = 9$ is applied for all of the simulations. XFOIL permits the analysis of low Reynolds number flows [**13**], and the code has been well tested at $Re \geqslant 2 \times 10^5$. It can, however, encounter problems when considering lower Reynolds number flows: although it is able to take into account laminar separation bubbles, it tends to under-predict the drag coefficient and over-predict the lift coefficients. Furthermore, if complete laminar separation occurs, then XFOIL is unable to converge [**11–13**].

A typical chord Reynolds number for the studied eagle is of the order $Re = 1.5 \times 10^5$, which has been bracketed here by also running computations at $Re = 1 \times 10^5$ and 2×10^5. Because these Reynolds numbers fall below the range in which XFOIL is known to be well behaved, the code was first validated by predicting the lift and drag coefficients of two technical aerofoil sections, namely Selig S1223 and Clark Y, and by comparing these with the results of published wind tunnel measurements at comparable Reynolds numbers [**14**, **15**]. Selig S1223 was chosen for comparison, because it was specifically designed for high-lift coefficient above $C_{\text{Lmax}} = 2$ at $Re = 2 \times 10^5$ [**16**]. The Clark Y was selected as a generic baseline aerofoil, because it is among the most widely tested of all sections and is not specifically optimized for either low Reynolds number flows or high-lift coefficients [**17**].

3 RESULTS AND DISCUSSION

3.1 Shape of bird-wing aerofoil sections

The arm wing of the eagle is arched strongly upwards during the rapid pitch-up manoeuvre (Figs 1 and 4). The arm wing is swept forward (Fig. 2) and is twisted in a positive sense from the root to the tip (i.e. has a wash-in distribution), which is expected to contribute to the aerodynamic stability of the bird [**18**]. The measured aerofoil sections (Fig. 5, Table 1) are unusual in comparison with technical aerofoil sections. Although their high degree of camber is comparable with that of technical aerofoils specifically engineered for high-lift low-Reynolds number applications, the bird-wing aerofoil sections combine this with an unusually thick leading edge and a trailing plate-like portion that is sufficiently thin and flexible to acquire reflex camber under positive aerodynamic loading (Fig. 5). The general shape of the bird-wing aerofoils shows a degree of similarity to the Jedelsky and Benedek profiles [**19**] that have been used in small model aircraft design; these sections also have a thicker leading edge portion with a plate-like trailing portion.

The reconstructed wing is based upon a single instance (Fig. 1) of the rapid pitch-up manoeuvre that occurs at the end of a typical gliding perching sequence [**7**]. This is a dynamic manoeuvre, during which the wing is pitching and morphing simultaneously. The upper surface feather deflections are indicative of flow separation and these feathers have

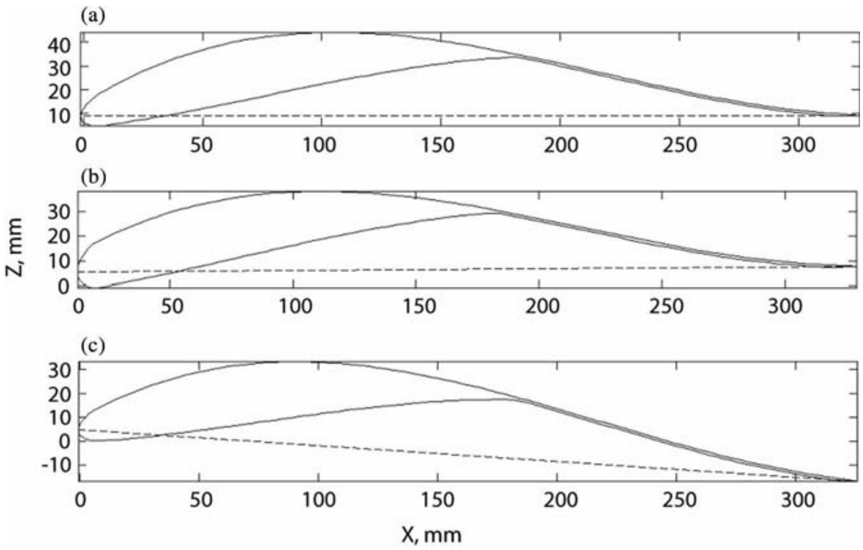

Fig. 5 (a) Standard bird-wing aerofoil section; (b) squashed bird-wing aerofoil section at 35 per cent of the span; and (c) elongated bird-wing aerofoil section at 84 per cent of the span. Chord lines are indicated using dashed lines and sections are shown with spanwise position wing twist

Table 1 Profile geometries for bird-wing aerofoil sections including the camber-to-chord ratio (δ/c), thickness ratio (t/c), and leading edge radius ratio (r/c), respectively

Section	δ/c (%)	t/c (%)	r/c (%)
Standard	8.2	7.7	1.19
Squashed	7.7	8.0	1.95
Elongated	8.1	7.8	1.15

deliberately not been included in the reconstruction (Fig. 2) because their deflection is rather chaotic and they do not give a good indication of the underlying shape of the wing. Instead, data points to either side of the deflected feathers have been included in the reconstruction to allow interpolation across regions of the wing experiencing separated flow. The wing reconstruction presented here is therefore intended to be representative of a baseline aerofoil section, although the actual aerofoil section might be much more rugged at high angles of attack, when the flow is unsteady and may be separated.

3.2 Comparative performance of bird-wing aerofoil sections

3.2.1 Technical aerofoil sections

Although the 3D shape of the arm wing has been measured, reconstruction of the more complicated geometry of the outer portion of the wing, including the tip feathers, was not attempted. Therefore the aerodynamic analysis presented here has been restricted to a 2D analysis of aerofoil sections from the arm wing, because a 3D aerodynamic analysis of the arm wing alone is unlikely to capture correctly the full complexity of the 3D flow. Furthermore, because the aim of this article is to provide baseline data for bird-wing aerofoils, the analysis has been restricted to steady flow conditions. It is therefore important to emphasize that the measurements made in this article are intended to be understood as characterizing the measured aerofoil sections, rather than the wing of the bird *per se*.

XFOIL results for the two technical aerofoils, Clark Y and S1223, were compared against the available 2D wind tunnel data taken from the University of Illinois at Urbana-Champaign (UIUC) Airfoil Coordinates free-source online database [**14**, **15**]. While the wind tunnel data do not cover the full range of combinations of Reynolds number and angle of attack tested here, the shapes of the measured lift and drag polars (Fig. 6) are in good agreement with those predicted using XFOIL. In particular, the gradients of the curves match closely, although XFOIL over-predicts the absolute lift coefficient and under-predicts the absolute drag coefficient, as is expected at such low Reynolds numbers. These effects are much more pronounced for Selig S1223, particularly at the highest angles of attack, although it should be borne in mind that S1223 was specifically designed using similar panel codes to have high lift and low drag at low Reynolds numbers [**16**]. In this sense, S1223 may be expected to serve as the ‘worst-case’ scenario for showing up the biases

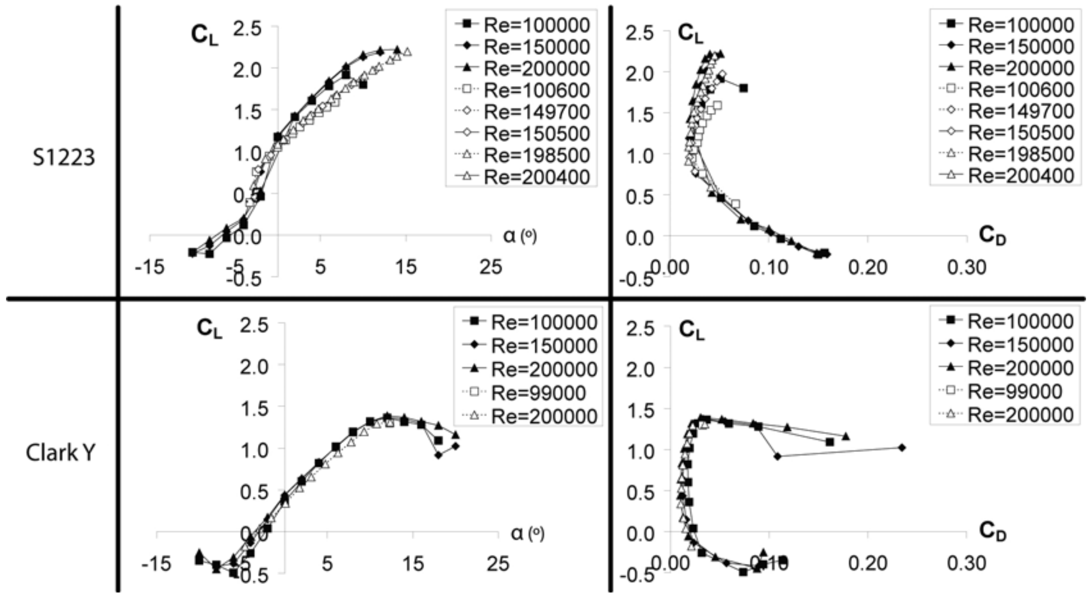

Fig. 6 Lift and drag polars for technical aerofoils shown as a comparison between XFOIL results (filled symbols) and wind tunnel data (open symbols) taken from the University of Illinois at Urbana-Champaign airfoil coordinates online database [**14**, **15**]

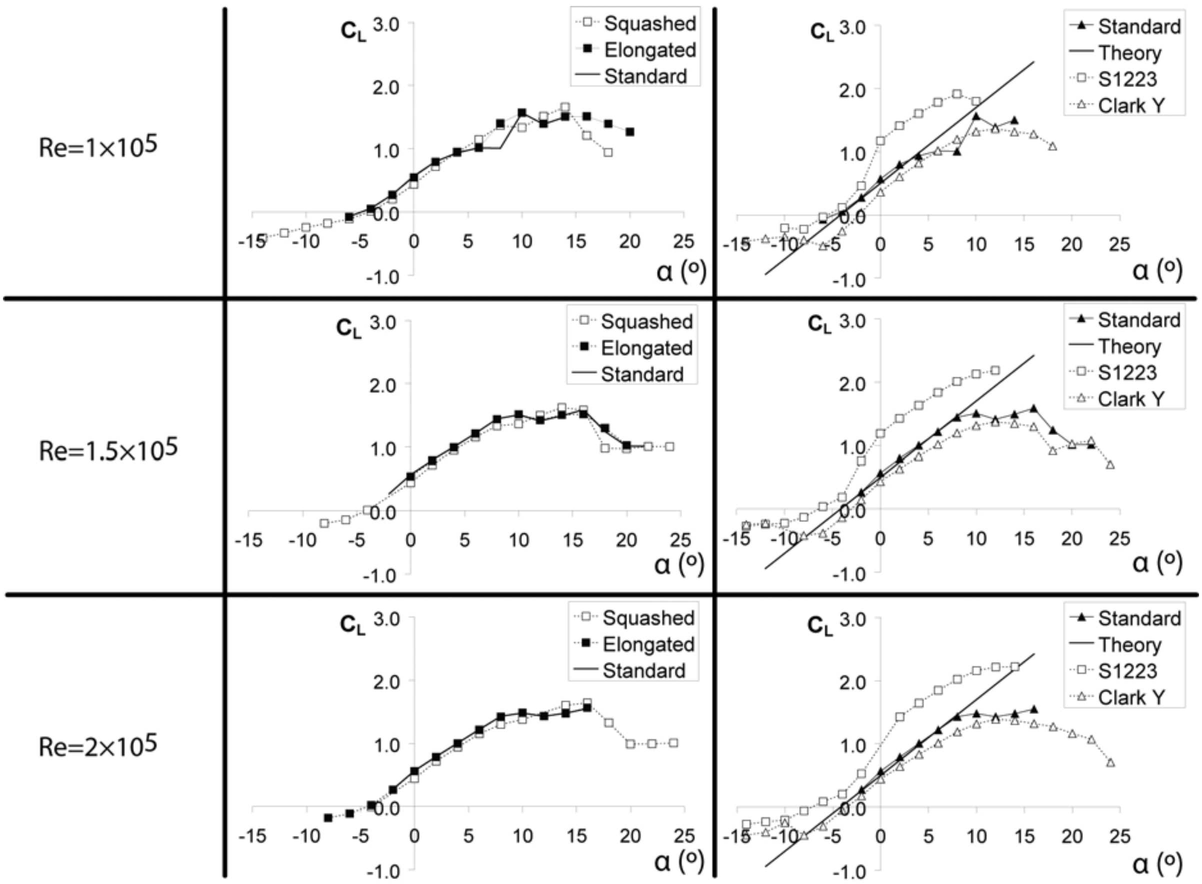

Fig. 7 Lift polars for bird-wing aerofoil sections, computed using XFOIL. Left column: results for the standard, squashed and elongated bird-wing aerofoil sections. Right column: results for the standard bird-wing aerofoil, Selig S1223 aerofoil, and Clark Y aerofoil. The straight line on each graph shows the slope predicted for a 2D aerofoil by thin aerofoil theory and is shown with arbitrary offset [**22**]

of over-prediction of lift and under-prediction of drag when using panel codes at low Reynolds numbers. The predicted results for the Clark Y aerofoil, which were not designed using panel codes, are much closer to the measured wind tunnel results. In any case, the results for the Selig S1223 and Clark Y aerofoils indicate that XFOIL may be assumed to provide reasonable qualitative, if not quantitative, estimates of aerofoil performance at the low Reynolds numbers considered here.

A further high-lift, low-Reynolds number aerofoil, the Eppler E423, which has been used as an approximation to a bird-like aerofoil by Jones *et al.* [**20**], is also considered in the present article. However, both the wind tunnel [**21**] and the XFOIL results for this section were extremely sensitive to slight variations in angle of attack, to such a degree that the unmeasured aerofoil surface roughness or freestream turbulence would have had a significant effect upon the results. Therefore the results for the Eppler E423 are not presented here.

3.2.2 Bird wing sections

Figures 7 and 8 plot the predicted lift and drag polars for the standard bird-wing aerofoil section, alongside the squashed and elongated aerofoil sections at 35 per cent and 84 per cent of the reconstructed wing span, respectively. The 2D aerofoil lift curve slope $\partial C_L / \partial \alpha = 2\pi$ predicted by thin aerofoil theory [**22**] is plotted for comparison on the same axes, with the lift coefficient at zero angle of attack set arbitrarily at $C_{L0} = 0.5$. The bird wing sections have a lift curve slope that is close to the theoretical 2D lift curve slope (Fig. 7). The standard bird wing sections show a stall angle at approximately $\alpha = 14°$.

Laminar separation bubbles are observed at $Re = 1 \times 10^5$, indicated by the sharp spike in the drag polars, for both the standard and elongated aerofoil sections at $\alpha = 8°$ (Fig. 8), but not in the case of the squashed aerofoil. As the Reynolds number increases, the lift and drag polars show closer agreement between the standard and stretched sections. This indicates that

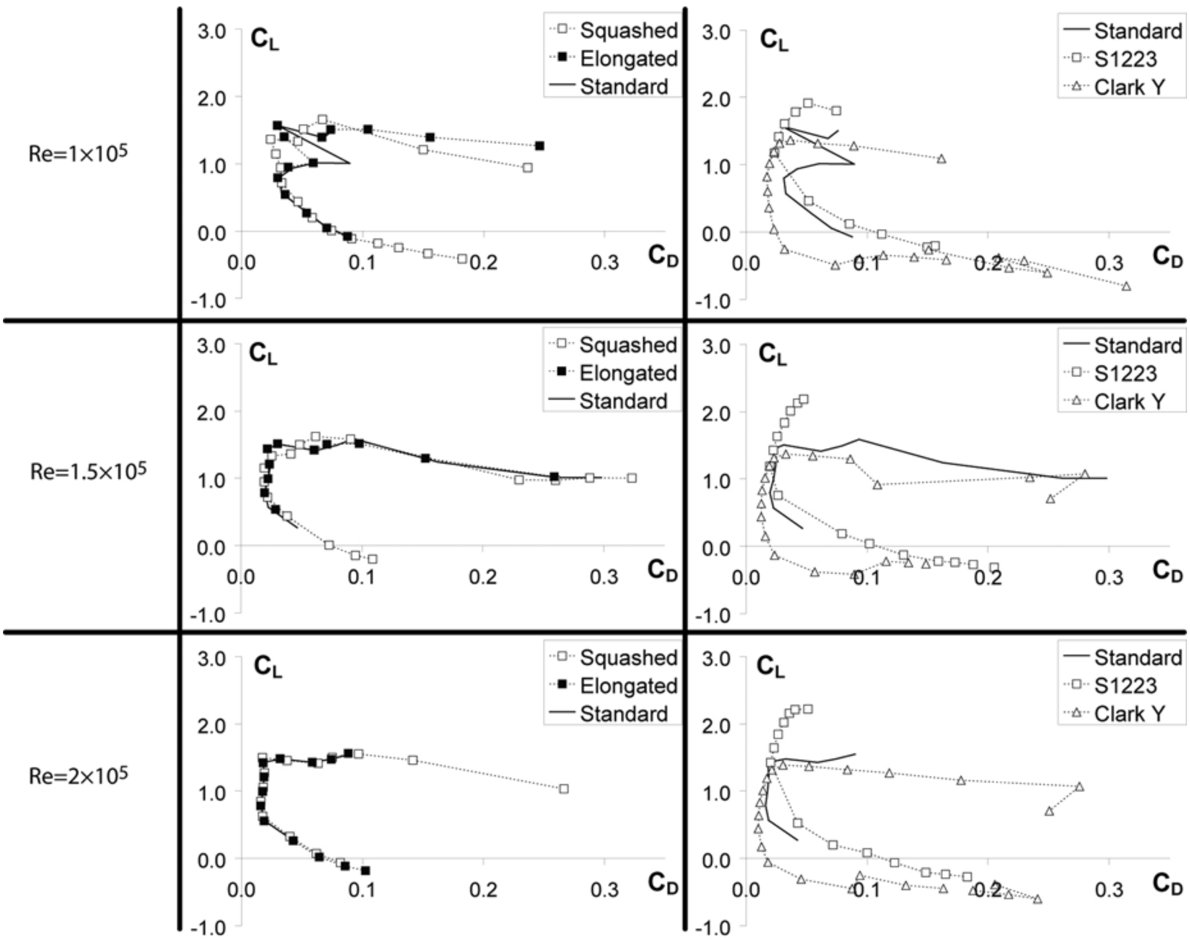

Fig. 8 Drag polars for bird-wing aerofoil sections, computed using XFOIL. Left column: results for the standard, squashed and elongated bird-wing aerofoil sections. Right column: results for the standard bird-wing aerofoil, Selig S1223 aerofoil, and Clark Y aerofoil

at lower Reynolds numbers the lift and drag polars become increasingly sensitive to variations in aerofoil shape. Laminar separation bubbles are not observed on either of the technical aerofoils at any of the Reynolds numbers tested.

Comparing the S1223, Clark Y and standard bird aerofoils, all three have a fairly wide drag-bucket (region of minimum drag), where C_D is low across a range of values of C_L. This drag-bucket is found at higher C_L for S1223, at lower C_L for Clark Y, and at intermediate C_L for the standard bird aerofoil. The absolute maximum lift-to-drag ratio (L/D) is highest for S1223, and is lowest for Clark Y. The standard bird aerofoil achieves a respectable maximum $L/D = 78.7$ at $C_L = 1.43$ (at $Re = 2 \times 10^5$). The minimum drag for the standard bird aerofoil lies between that of the two technical aerofoils (Clark Y: $C_{Dmin} = 0.0102$, S1223: $C_{Dmin} = 0.0196$ versus the bird section: $C_{Dmin} = 0.0161$). The region of minimum drag is marginally wider for the technical aerofoils than for the bird aerofoil (i.e. close to minimum drag is achieved over a wider range of C_L values), but the bird aerofoil has the interesting property of maintaining nearly constant C_D across a wide range of C_L values (e.g. $Re = 2 \times 10^5$, $C_D = 0.0182$–0.0187 from $C_L = 1.43$ to 0.57, respectively).

Although the bird wing section outperforms the Clark Y aerofoil, it does not perform as well as the S1223 aerofoil, which has been specifically engineered for maximum lift at these transitional Reynolds numbers. The bird's wing has, instead, evolved to perform well under a wide range of different flight regimes at transitional Reynolds numbers. Unlike these technical sections, the bird must be able to perform well under the steady conditions of fixed-wing gliding, as well as in a range of highly unsteady conditions including the landing manoeuvre that has been considered here, and the flapping motions associated with powered flight. The lift and drag polars indicate that bird aerofoil design is robust and relatively insensitive to slight variations in turbulence and surface roughness. Finally, it should be noted that while the present article has analysed the bird aerofoil as if it had smooth surfaces (to allow comparison with the technical aerofoils), in real life feathers are very rough, even when they are in the resting position: nothing is known about the boundary layer properties of real bird wings.

4 CONCLUSIONS

This article has presented a bird wing reconstruction measured from an eagle in free flight in its natural environment, during a gliding landing. Multiple camera photogrammetry has been used to reconstruct 3D data points by digitization of natural markers on the wing. Statistical techniques were then used to generate the upper and lower surfaces of the inner wing. Aerofoil sections from the standard, elongated, and squashed sections from the final wing were analysed at Reynolds numbers in the range $1 \times 10^5 \leqslant Re \leqslant 2 \times 10^5$ and were compared to two technical aerofoils. The standard bird-wing aerofoil section does not perform as well as the high-lift low Reynolds number S1223 aerofoil, but has a wide angle of attack range over which the drag remains low.

ACKNOWLEDGEMENTS

The authors thank their falconers Martin Cray and Joseph Binns for their assistance during experiments. The research leading to these results has received funding from the European Research Council under the European Community's Seventh Framework Programme (FP7/2007-2013)/ERC grant agreement no. 204513. This research effort was also sponsored by the Air Force Office of Scientific Research, Air Force Material Command, USAF, under grant number FA8655-05-1-3077. The US Government is authorized to reproduce and distribute reprints for Governmental purpose notwithstanding any copyright notation thereon. The authors gratefully acknowledge additional support from the Hester Cordelia Parsons Fund, Oxford University. ACC received a Royal Commission for the Exhibition of 1851 Brunel Research Fellowship during the course of this research. GKT received a Royal Society University Research Fellowship and is currently an RCUK Academic Fellow.

REFERENCES

1 **Withers, P. C.** An aerodynamic analysis of birds wings as fixed aerofoils. *J. Exp. Biol.*, 1981, **90**, 143–162.

2 **Liu, T., Kuykendoll, K., Rhew, R.,** and **Jones, S.** Avian wing geometry and kinematics. *AIAA J.*, 2006, **44**, 954–963.

3 **Nachtigall, W. N.** and **Wieser, J.** Profilmessungen am Taubenflügel. *Zeitschrift für vergleichende Physiologie*, 1966, **52**, 333–346.

4 **Bilo, D.** Flugbiophysik von Kleinvögeln. I. Kinematik und Aerodynamik des Flügelabschlages beim Haussperling (Passer domesticus L.). *Z. vergl. Physiol.*, 1971, **71**, 382–454.

5 **Bilo, D.** Flugbiophysik von Kleinvögeln. II. Kinematik und Aerodynamik des Flügelaufschlages beim Haussperling (Passer domesticus L.). *Z. vergl. Physiol.*, 1972, **76**, 426–437.

6 **Brill, C., Mayer-Kunz, D. P.,** and **Nachtigall, W.** Wing profile data of a free-gliding bird. *Naturwissenschaften*, 1989, **76**, 39–40.

7 **Carruthers, A. C., Thomas, A. L. R.,** and **Taylor, G. K.** Automatic aeroelastic devices in the wings of a steppe eagle *Aquila Nipalensis*. *J. Exp. Biol.*, 2007, **210**, 4136–4139.

8 **Walker, S. W., Thomas, A. L. R.,** and **Taylor, G. K.** Photogrammetric reconstruction of high-resolution surface topographies and deformable wing kinematics of tethered locusts and free-flying hoverflies. *J. R. Soc. Interface*, 2009, **6**, 351–366.
9 **Atkinson, K. B.** *Close range photogrammetry and machine vision*, 1996 (Reinhold, New York).
10 XFOIL, available from http://web.mit.edu/drela/Public/web/xfoil/.
11 **Liu, T., Kuykendoll, K., Rhew, R.,** and **Jones, S.** Avian wing geometry and kinematics. *AIAA J.*, 2006, **44**, 954–963.
12 **Genç, M. S., Kaynak, Ü.,** and **Lock, G. D.** Flow over an aerofoil without and with a leading-edge slat at a transitional Reynolds number. *Proc. IMechE, Part G: J. Aerospace Engineering*, 2009, **223**, 217–231. DOI: 10.1243/09544100JAERO434.
13 Designing an airfoil, available from http://www.mh-aerotools.de/airfoils/methods.htm.
14 **Selig, M. S., Guglielmo, J. J., Broeren, A. P.,** and **Giguere, P.** *Summary of low-speed airfoil data*, vol. 1, 1995 (SoarTech Aero Publications, Virginia Beach, Virginia, 23451, USA), available from http://www.soartech-aero.com/, herkstok@aol.com.
15 **Lyon, C. A., Broeren, A. P., Giguere, P., Gopalarathnam, A.,** and **Selig, M. S.** *Summary of low-speed airfoil data*, vol. 3, 1997 (SoarTech Aero Publications, Virginia Beach, Virginia, 23451, USA), available from http://www.soartech-aero.com/, herkstok@aol.com.
16 **Selig, M. S.** and **Gulielmo, J. J.** High-lift low Reynolds number airfoil design. *J. Aircr.*, 1997, **34**(1), 72–79.
17 **Marchman, J. F.** and **Werme, T. D.** Clark-Y airfoil performance at low Reynolds numbers. In Proceedings of the AIAA 22nd Aerospace Sciences Meeting, Reno, Nevada, USA, 9–12 January 1984, AIAA paper 84-0052.
18 **Thomas, A. L. R.** and **Taylor, G. K.** Animal flight dynamics I. Stability in gliding flight. *J. Theor. Biol.*, 2001, **212**, 399–324. DOI:10.1006/jtbi.2001.2387.
19 **Simons, M.** *Model aircraft aerodynamics*, 3rd edition, 1994 (Argus Books, Hemel Hempstead, UK).
20 **Jones, A. R., Bakhtian, N. M.,** and **Babinsky, H.** Low Reynolds number aerodynamics of leading edge flaps. *J. Aircr.*, 2008, **45**(1), 342–345.
21 **Selig, M. S., Guglielmo, J. J., Broeren, A. P.,** and **Giguere, P.** *Summary of low-speed airfoil data*, vol. 2, 1996 (SoarTech Aero Publications, Virginia Beach, Virginia, 23451, USA), available from http://www.soartech-aero.com/, herkstok@aol.com.
22 **Shevell, R. S.** *Fundamentals of flight*, 1983 (Prentice-Hall, Inc., New Jersey, USA).

APPENDIX

Notation

c	aerofoil section chord
C_D	drag coefficient
C_{Dmin}	minimum drag coefficient
C_L	lift coefficient
C_{Lmax}	maximum lift coefficient
C_{L0}	lift coefficient at $\alpha = 0°$
D	drag force
L	lift force
N_{crit}	XFOIL amplification factor for transition prediction
r	leading edge radius
Re	Reynolds number
t	maximum aerofoil thickness
X	chordwise position on the wing
Y	spanwise position on the wing
Z	height of the point on the wing
α	angle of attack
δ	maximum height of the camber line above the chord